A major purpose of the Technical Information Center is to provide the broadest dissemination possible of information contained in DOE's Research and Development Reports to business, industry, the academic community, and federal, state and local governments.

Although a small portion of this report is not reproducible, it is being made available to expedite the availability of information on the research discussed herein.

LA-UR-83-69

Conf-830301--6

LA-UR--83-69

DE83 006064

TITLE A TWO-DIMENSIONAL NUMERICAL MODEL OF UNDERGROUND OIL-SHALE RETORTING

AUTHOR(S) Bryan J. Travis, ESS-5

Paul J. Hommert and Craig E. Tyner, Sandia National Laboratories

SUBMITTED TO Session on Underground Conversion, ASME/JSME Thermal Engineering Conference, Honolulu, Hawaii, March 20-24, 1983.

Los Alamos Los Alamos National Laboratory
Los Alamos, New Mexico 87545

A TWO-DIMENSIONAL NUMERICAL MODEL OF UNDERGROUND OIL SHALE RETORTING

Bryan J. Travis
Earth and Space Sciences Division
Los Alamos National Laboratory
Los Alamos, New Mexico 87545

and

Paul J. Hommert and Craig E. Tyner
Geo Energy Technology Department
Sandia National Laboratories
Albuquerque, New Mexico 87131

ABSTRACT

A two-dimensional numerical model of underground oil shale retorting, which fully couples retorting chemistry with fluid and heat flow, has been developed. The model solves the time-dependent, two-dimensional mass, momentum, and energy balance equations for a nine-component fluid (O_2, N_2, H_2, CO_2, CO, CH_4, CH_x, H_2O, and oil). Water and oil can flow in the liquid and/or vapor phases. Retort chemistry includes kerogen pyrolysis, carbonate decomposition, char reactions, and combustion. Also, detailed modeling of heat flow and chemistry inside shale particles allows large rubble sizes as well as small sizes to be considered.

The model is compared to one-dimensional experimental data obtained from Lawrence Livermore National Laboratory. The model can be used to examine the effect of two-dimensional variations in shale grade, rubble size, permeability, porosity, geometry, inflow gas composition, etc. on retorting efficiency and process optimization. A sample calculation is presented.

NOMENCLATURE

C	concentration of chemical specie	(kg/kg)
E	energy source or sink rate	(J/s)
H	heat of reaction	(J)
I	internal energy per unit volume	(J/m^3)
K	reaction rate coefficients	(s^{-1})
K_D	mass transfer coefficient	(m/s)
L	average local particle size	(m)
M	molecular weight	(gm/mole)
N_i	number of particles of radius R_{pi}	
P	fluid pressure	(kPa)
R	particle radius	(m)
Re	Reynold's number	
Ro	gas constant	(J/mole · K)
S	mass source or sink rate	(kg/s)
T	temperature	(k)
V	velocity	(m/s)
W_i	weight percent of particles having radius R_{pi}	
X	mole fraction in bulk gas	
f	fraction of void space occupied by air and vapor	
$\vec{g}$	gravity acceleration	(m/s^2)
k	effective permeability	(m^2)
r	radial position within a particle	(m)
t	time	(s)
n	molar density	
α	stoichiometric coefficients	
β	heat transfer coefficient between fluid and particles	($J/m^2/s$)
δ	Dirac delta functional	
ϵ	porosity	
λ	thermal conductivity	(J/m °C s)
μ	viscosity	(kg/m s)
ρ	mass density	(kg/m^3)
σ	fraction of void space occupied by liquid	
Ω	computational cell volume	(m^3)

Subscripts

c	refers to char
f	refers to total fluid
g	refers to gas component
gv	refers to gas-vapor mixture
i	refers to phase (liquid or air/vapor)
ij	refers to j^{th} specie involved in i^{th} chemical reaction
j	refers to j^{th} gas component
ℓ	refers to liquid
p	refers to properties of a representative particle
pi	refers to property of i^{th} representative particle
q	refers to a chemical specie inside particles
s	refers to average value on particle surface
si	refers to surface of particle size i
v	refers to vapor component

INTRODUCTION

Huge reserves of hydrocarbons lie locked in shale deposits under the Rocky Mountains. Economically feasible extraction of this fossil resource is a difficult task. Several schemes have been proposed. One important class of extraction methods is the in situ approach. Here, porosity is created in shale by partial mining followed by blasting,

The resulting rubble is then burned in place to drive out oil and various gas products from the shale rubble. Oil yield depends on many factors, for example, how uniformly the shale is rubbled, what ignition strategy is used, etc.

Field and laboratory experiments are needed to define the dependence of oil yield on various parameters. However, field experiments are quite expensive. Experimentally validated mathematical models of the retorting process can be helpful by allowing various parameters to be manipulated in the computer at much less expense. Models also provide a framework for analyzing experimental results and can provide guidance in the design of experiments and process optimization.

Several models of oil shale retorting have been published in the last decade. The most detailed and documented is Braun's model (1). Almost all of the models available are one-dimensional. The two-dimensional work available either treats only a specialized geometry with one-dimensional flow (2) or does not contain a full chemistry model coupled with a complete description of the flow (3). They cannot properly handle the non-uniformities that will inevitably arise.

Non-uniformities in in situ retorts can be of several types: those due to spatial variations in shale grade; those due to variations in rubble size, porosity, etc., brought about by blasting; and those due to asymmetric injection/collection. These non-uniformities will frequently be multi-dimensional and extensive (4). The evaluation of the sensitivity of a retorting process to various non-uniformities requires a multi-dimensional retorting model. Because of these considerations, we have constructed a transient, two-dimensional model of oil shale retorting that fully couples fluid dynamics to retort chemistry.

A fully coupled, two-dimensional MIS (modified in situ) oil shale retorting model will allow us to examine the influence of spatial variations in shale rubble permeability, porosity, grade, and rubble size on retorting efficiency. The effects of retort geometry, air injection, and ignition strategies can also be considered. For example, the model could possibly be used to find an air injection/inflow composition strategy that would minimize the adverse effects of poorly rubbled regions. Gravitational effects, which are especially important in horizontal retorting since hot injection gases and combustion products will tend to rise to and flow along the top of a horizontal shale layer, are included. Condensation of steam and particularly of oil vapor may also be an important process. Reference (5) argues for the timeliness of pursuing this task.

Our approach to this modeling effort consists of taking a fairly detailed porous flow model called WAFE (6), the first version of which was written in 1977, and adding to it the oil shale chemistry that has been worked out at the Lawrence Livermore National Laboratory (LLNL) (7). The expanded version of WAFE is called WAFE-OS (8), the details of which we now describe.

WAFE-OS MODEL

Flow

The WAFE-OS code models transient, multi-phase, multi-component, two-dimensional mass and heat transport in porous media using Cartesian or cylindrical coordinates. Flow is not restricted to Darcy's law. This allows us to compute flows in high permeability regions and channels. Material properties of the shale, such as porosity, permeability, conductivity, etc., and initial conditions can vary spatially. Horizontal and vertical anisotropy is also allowed. Boundary conditions and mass and energy sources and sinks can be constant or time-dependent. Sources/sinks can be specified in any number of computational zones. The inclusion of gravity allows us to examine buoyancy-dominated flows. The code employs a highly implicit, integrated finite difference numerical scheme.

WAFE-OS solves the conservation equations of mass, momentum and energy for flow in porous media. Currently, WAFE-OS carries two condensable components (H_2O, oil) and seven noncondensable gases (O_2, N_2, H_2, CO_2, CO, CH_x, CH_4). The mass conservation equation for a noncondensable is

$$\epsilon\, \partial_t(f\rho_g) + \nabla \cdot \rho_g \vec{V}_g = \epsilon \dot{S}_g \qquad (1)$$

and, for a condensable component,

$$\epsilon\, \partial_t(\rho_\ell\, \sigma + \rho_v\, f) + \nabla \cdot (\rho_\ell \vec{V}_\ell + \rho_v \vec{V}_v) = \epsilon \dot{S}_{\ell v} \quad . \qquad (2)$$

The momenta equations are carried in a reduced form known as the Forchheimer equation (9)

$$\left(1 + \frac{.01}{1-\epsilon}\frac{\rho_i L |\vec{V}_i|}{\mu_i}\right)\vec{V}_i = -\frac{k_i}{\mu_i}(\nabla P_i + \rho_i \hat{g}) \quad . \qquad (3)$$

This relation takes into account inertial effects but not acceleration. It can also be written as an expansion in Reynold's number, Re,

$$\left(1 + \frac{.01}{1-\epsilon}\mathrm{Re}_i\right)\vec{V}_i = \vec{V}_{Di} \quad , \qquad (4)$$

where $\vec{V}_{Di}$ is the Darcy equation velocity for phase i. At low Reynold's numbers ($\lesssim 10$), this reduces to Darcy's law.

The WAFE-OS model carries an energy equation for the fluid and a separate one for the matrix. For the fluid, the change in internal energy depends on the energy convected in the liquid and gaseous phases, on energy sources/sinks, on the work done on and by the fluid as it flows, on the exchange of energy between the fluid and the rock, and finally on thermal diffusion in the fluid. The fluid energy equation is

$$\epsilon\frac{\partial(fI_{gv} + \sigma I_\ell)}{\partial t} + \nabla \cdot \left(I_{gv}\vec{V}_{gv} + I_\ell \vec{V}_\ell\right) = \epsilon F_f - \epsilon P_f \nabla \cdot \vec{V}_f$$
$$+ \nabla \cdot \epsilon\lambda_f \nabla T_f - \sum_i \frac{3(1-\epsilon)a(T_f - T_{si})w_i}{R_{pi}} \quad , \qquad (5)$$

where λ_f is the effective thermal conductivity for the fluid and is computed from

$$\lambda_f = \sigma\lambda_\ell + f\lambda_{gv} \quad . \qquad (6)$$

The energy conservation for the rock is somewhat more complicated. For the purpose of energy calculation, the shale inside a computational zone is assumed to be in the form of spherical particles. The actual distribution of particle sizes in a computational zone is approximated by no more than five representative particles of radii R_{pi}. Care must be taken to insure that the actual volume of shale and the total

surface area are truly represented by proper choice of R_{pi} and W_i. R_{pi} can vary from zone to zone. The energy equation for each zone's representative particle includes heat diffusion within the particle, heat of reaction from chemical reactions inside the particle, and a source term Q, which is the energy conducted from one zone to the next. At the surface of each particle, heat exchange with the fluid occurs. The rock energy conservation is stated in the following equations:

$$\partial_t I_p = \frac{1}{r^2}\frac{\partial}{\partial r}\left(r^2 \lambda_p \frac{\partial T_p}{\partial r}\right) + \sum_q H_q \partial_t C_q + \delta(r - R_p)\, 4\pi R_p^2 Q \quad , \tag{7}$$

$$Q = \frac{1}{4\pi \sum_i N_i R_{pi}^2} \int_{\substack{\text{all particles} \\ \text{in } \Omega}} \nabla \cdot \left[(1-\epsilon)\lambda_p \nabla T_s\right] d\Omega \quad , \tag{8}$$

$$\lambda_p \frac{\partial T_p}{\partial r} = \beta (T_f - T_{si}) \text{ at } r = R_{pi} \quad , \tag{9}$$

$$\partial_t C_q = \sum_j \alpha_{qj} K_{qj}(T_p) C_j \quad , \tag{10}$$

The gas products generated inside particles along with the associated energies are deposited in the fluid in the porosity via the mass and energy source/sink terms in equations (1), (2), and (5).

Several constitutive relations are needed to complete the model. Effective permeability for each phase depends on saturation, pressure, and location. Fluid viscosities are functions of temperature and, for the gas phase, of mole fractions. Tables are used for much of the condensable component equation of state; noncondensables are treated as perfect gases. Finally, the sum of all saturations must equal one. These relations are summarized in the following expressions:

$$k_i = k_i(\sigma_i, P_i, \bar{x}) \quad , \tag{11}$$

$$\mu_i = \mu_i(T_f, n_{i1}, n_{i2}, n_{i3}, \ldots, n_{ij}) \quad , \tag{12}$$

$$I = I(T_f, \rho_\ell, \rho_v, \rho_{g1}, \rho_{g2}, \ldots, \rho_{gj}) \quad , \tag{13}$$

$$\rho_g = \sum_j \rho_j \frac{R}{M_j} T_f, \; P_v = P_v(T_f, \rho_v, \sigma) \quad , \tag{14}$$

$$f + \sigma_{oil} + \sigma_{H_2O} = 1 \quad , \tag{15}$$

WAFE-OS is completely operational. Total mass and energy are conserved during mass and energy exchange between the particles and the fluid. Shale particles can have up to ten internal shells for energy and chemistry calculations, but the total number of shells per zone cannot exceed 10 because of computer memory limitations. There are a few minor changes planned in the future, for example, allowing λ_p to depend on T_p. A typical computational mesh is shown in Fig. 1. Also shown are the representative shale particles and their internal structure.

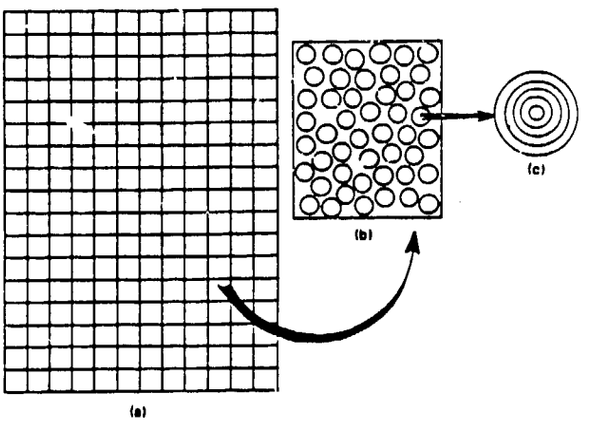

Fig. 1. Typical computational mesh (a), zone (b), and particle (c).

Derivation of the equations of flow, Eqs. (1)-(5), for a permeable medium and a discussion of underlying assumptions can be found in Ref. (10).

Kerogen

The kerogen decomposition model is similar to that described in Ref. (7) and is summarized here. Oil and C_2 and C_3 compounds are released in one step. CH_4 and H_2, however, are released in several steps, each corresponding to a temperature range.

The basic stoichiometry for western oil shale kerogen pyrolysis is:

Primary kerogen pyrolysis ($T < 500^\circ C$) (16)

$$\text{Kerogen} \rightarrow .725 \text{ oil} + .205 \text{ char}_1 + .018 \text{ CO}_2 + .011 \text{ H}_2 + .008 \text{ CH}_4 + .014 \text{ CH}_x + .017 \text{ H}_2\text{O}$$

Secondary char pyrolysis ($500 < T < 650^\circ C$) (17)

$$\text{Char}_1 \rightarrow .952 \text{ char}_2 + .047 \text{ CH}_4 + .068 \text{ H}_2$$

Additional char pyrolysis ($650 < T < 900^\circ C$) (18)

$$\text{Char}_2 \rightarrow \text{char}_3 + .13 \text{ H}_2$$

3.7×10^5 J/kg kerogen are absorbed.

The temperature dependence of the rate "constants" has been modified from that given in Ref. (7) to allow us to fit kerogen pyrolysis data without resorting to a distribution of activation energies for H_2 and CH_4.

The actual steps used to describe kerogen and char pyrolysis in WAFE-OS are:

$$\text{Kerogen} \begin{cases} \xrightarrow{K_{11}} \text{oil, char}_1, \text{CO}_2, \text{H}_2\text{O}, \text{CH}_x \\ \xrightarrow{K_{12}} \text{H}_2 \\ \xrightarrow{K_{13}} \text{CH}_4 \end{cases} \tag{19}$$

$$\text{Char}_1 \begin{cases} \xrightarrow{K_{21}} & \text{char}_2,\ H_2 \\ \xrightarrow{K_{22}} & CH_4 \end{cases} \quad (20)$$

$$\text{char}_2 \xrightarrow{K_3} \text{char}_3,\ H_2 \quad (21)$$

where the rate coefficients K_i are given by

$$K_{11} = 2.8 \times 10^{13} \times e^{(-26341/T)}\ s^{-1} \quad (22)$$
$$K_{12} = 1.1 \times 10^{10} \times e^{(-22011/T)}\ s^{-1} \quad (23)$$
$$K_{13} = 5.8 \times 10^{9} \times e^{(-20568/T)}\ s^{-1} \quad (24)$$
$$K_{21} = 13{,}000 \times e^{(-14554/T)}\ s^{-1} \quad (25)$$
$$K_{22} = 3.1 \times e^{(-8359/T)}\ s^{-1} \quad (26)$$
$$K_3 = 29 \times e^{(-12028/T)}\ s^{-1} . \quad (27)$$

The oil released in primary kerogen pyrolysis can exist as liquid and vapor in a certain temperature range. In WAFE-OS, the partitioning of oil between the liquid and vapor states is accomplished in the following manner.

$$\text{oil (vapor)} = x \cdot \text{oil}$$
$$\text{oil (liquid)} = (1 - x) \cdot \text{oil} \quad (28)$$

where

$$x = \begin{cases} 0.38\ , & \text{for } T < 490\ K \\ 0.38 + (T - 490) * 0.0021908\ , & \text{for } 490 < T < 773\ K \\ 1.\ , & \text{for } T > 773\ K. \end{cases} \quad (29)$$

Oil vapor is removed from a particle shell. Liquid oil remains behind. If, however, the heating rate in a particle shell is sufficiently large, more liquid oil will be vaporized. The total oil produced (and deposited into the gas stream) during a time step in a particle shell is given by

$$\text{oil (produced)} = \text{oil (vapor)} + \text{oil (liquid)} \times \min\left[1, \max\left(0, 0.12 \times \Delta T_p/\Delta t\right)\right] , \quad (30)$$

where $\Delta T_p/\Delta t$ is the rate at which the shell temperature is changing.

Carbonates

Two carbonates are allowed, calcite and dolomite. The calcite and dolomite decompositions are those described in Ref. (1), namely,

$$5\ CaCO_3 + 2\ SiO_2 \longrightarrow 2\ CaSiO_4 + CaO + 5\ CO_2 \quad (31)$$

$$MgCO_3 \longrightarrow MgO + CO_2 . \quad (32)$$

In the first reaction, 1. kg of $CaCO_3$ yields 0.44 kg of CO_2 and requires 2.9×10^6 J/kg CO_2. In the second reaction, 1. kg of $MgCO_3$ yields 0.522 kg of CO_2 and absorbs 3×10^6 J/kg CO_2. The rate coefficients for these reactions are

$$k_1 = 9.6 \times 10^{10}\ e^{(-36050/T)}\ s^{-1}. \quad (33)$$
$$k_2 = 1.7 \times 10^{10}\ e^{(-29090/T)}\ s^{-1}. \quad (34)$$

In the code, the percent composition of each carbonate can vary spatially.

Combustion

The true details of the gas stream combustion reactions are not known exactly. The following scheme provides a reasonable match with observations.

Reactions:

$$0.495\ \text{kg oil} + 1.\ \text{kg } C_2 \longrightarrow 0.507\ \text{kg } H_2O + 0.988\ \text{kg CO} \quad (35)$$

$$2\ H_2 + O_2 \longrightarrow 2\ H_2O \quad (36)$$

$$0.414\ \text{kg } CH_x + 1.\ \text{kg } O_2 \longrightarrow 0.608\ \text{kg } H_2O + 0.806\ \text{kg CO} \quad (37)$$

$$2\ CH_4 + 3\ O_2 \longrightarrow 4\ H_2O + 2\ CO \quad (38)$$

$$2\ CO + O_2 \longrightarrow 2\ CO_2 \quad (39)$$

The ignition temperature for these reactions is taken as 400°C. Above 400°C, gases are burned in the following order: oil, H_2, CH_x, CH_4, and CO. Combustion proceeds as far as the O_2 levels permit. These reactions are highly exothermic. The heats of reaction for the above reactions are:

$$H_1 = 0.988 \times 10^7\ J/kg\ O_2$$
$$H_2 = 1.51 \times 10^7\ J/kg\ O_2$$
$$H_3 = 1.08 \times 10^7\ J/kg\ O_2 \quad (40)$$
$$H_4 = 1.08 \times 10^7\ J/kg\ O_2$$
$$H_5 = 1.77 \times 10^7\ J/kg\ O_2$$

Char

The char/O_2 reaction can be an important source of heating for the retort process. The representative reaction is

$$C + O_2 \longrightarrow CO_2 \quad (41)$$

The heat of reaction is 3.28×10^7 J/kg char and is deposited in the particle shell zone containing the char burn front. We assume that char produced during kerogen pyrolysis is burned at a sharp interface as oxygen diffuses into the (assumed) spherical shale particles. This is the shrinking core model and agrees well with experimental data. The rate at which this sharp burn front moves inward is given by

$$\frac{dR_c}{dt} = -0.375\ \frac{[O_2]}{\rho_{char}} \left(\frac{R_c}{R_p}\right)^3 \left[\frac{1}{S_c\ k_6} + \frac{R_c(R_p - R_c)}{R_p\ D_e}\right]^{-1} \quad (42)$$

where

$[O_2]$ = gas stream oxygen density (kg/m^3)
ρ_{char} = local char density in particle shell (kg/m^3)
R_c = char burn-front radius (m)
S_c = specific surface area ($\approx 1000\ m^2/m^2$)
D_e = effective O_2 diffusivity in shale (m^2/s)
ρ_k^* = initial kerogen density (kg/m^3)

and

$$k_6 = 6.53 \times 10^5 \sqrt{T}\ e^{-22140/T}\ m/s \quad (43)$$

$$D_e = 1.04 \times 10^{-15}\ (\rho_k^*)^2\ T^{1.65}\ m^2/s . \quad (44)$$

The reaction can only proceed when O_2 and char are present. In addition, R_c is not allowed to change until the kerogen has been almost completely pyrolyzed (99% or more).

If char pyrolysis is not complete but the char O_2 reaction can occur, char pyrolysis is driven to completion in the particle shell volume swept out by R_c during a time step. This is also done for the other char reactions (char - CO_2 and char - H_2O).

The char/CO_2 reaction is

$$C + CO_2 \longrightarrow 2\ CO \quad . \tag{45}$$

Only the forward reaction is considered. This reaction requires high temperature (> 600°C) not only because of its own kinetics but also because it requires CO_2 that generally will be present only when carbonate decomposition is occurring, which requires elevated temperatures. This reaction is endothermic, absorbing 3.92×10^6 J/kg CO_2 consumed.

Sequencing of this reaction with other reactions is done in the following way. In each particle shell, the char/CO_2 reaction is not computed until kerogen decomposition is complete. If kerogen decomposition is complete, then carbonate decomposition is checked. If carbonate decomposition is occurring, the char/CO_2 reaction is calculated as follows.

The rate of CO_2 depletion, R_2 (kg/m^3 · s), is computed from

$$R_2 = \frac{k_c \rho_c}{F\left(1 + \dfrac{2\ R_2}{k_1(R_1 - R_2)}\right)} \quad . \tag{46}$$

R_2 is given by

$$R_2 = \frac{-B + \sqrt{B^2 + 4\ C}}{2} \quad , \tag{47}$$

where

$$B = \frac{(F\ R_1 + k_c\ \rho_c)k_1}{F(2 - k_1)} \quad , \quad C = \frac{k_c\ \rho_c\ k_1\ R_1}{F(2 - k_1)} \quad , \tag{48}$$

$$\begin{aligned} k_c &= 5.7 \times 10^4 \exp(-20130/T)\ (s^{-1}), \\ k_1 &= 4.15 \times 10^3 \exp(-11420/T)\ (s^{-1}), \\ F &= 0.2727\ \text{kg char/kg } CO_2\ (\text{kg/kg}), \\ \rho_c &= \text{local char concentration (kg/m}^3), \\ R_1 &= \text{rate of } CO_2 \text{ generation (kg/m}^3 \cdot \text{s}). \end{aligned} \tag{49}$$

For $k_1 < 2$, the solution for R_2 has two real roots, one positive and one negative; the positive root is taken. For $k_1 > 2$ (temperature $T > 1495$ K), the solution has no positive roots. In this case, we set $R_2 = 0$. At these temperatures, carbonate decomposition will be complete so CO_2 will not be present anyway. The char/CO_2 reaction should be important for temperatures between about 850 K and 1200 K.

After R_2 is known, adjustments in ρ_c and R_1 are required, namely,

$$R_1 \leftarrow R_1 - R_2 \quad , \tag{50}$$

$$\rho_c \leftarrow \rho_c - 12/44\ R_2\ \Delta t \quad , \tag{51}$$

where the arrow denotes replacement, and Δt is the time step. Finally, CO generation is given by

$$R_{CO} = 56/44\ R_2\ (\text{kg/m}^3 \cdot \text{s}) \quad . \tag{52}$$

Cnar - H_2O

$$C + H_2O \longrightarrow CO + H_2 \tag{53}$$

The char-steam reaction is controlled by three processes: transfer of steam from the bulk flow to a particle's surface, diffusion of steam into the particle, and the rate of reaction of steam with char.

Mass transfer from the bulk flow through a particle's surface is calculated from

$$\rho_{vp} = 3\ K_D\ \rho_v / R_p (1 + \lambda_{H_2O}) \quad , \tag{54}$$

where

$$K_D = 0.5\ V. \tag{55}$$

In equation (55), V is the magnitude of gas velocity.

Diffusion rate of H_2O vapor into shale is computed from

$$De,_{H_2O} = 7.4 \times 10^{-16}\ (\rho_K^\bullet)^2\ T^{1.73}\ (\text{m}^2/\text{s}) \quad , \tag{56}$$

where $\rho_K^\bullet$ is initial kerogen density (kg/m^3 shale). The transfer rate, which accounts to some degree for counterflow of gas from a particle and includes particle size effect, is

$$R_{7b} = \left[\frac{\ln(1 + X_{H_2O})}{X_{H_2O}}\right]\left[\frac{3\ De,_{H_2O}\ \rho_{vp}}{R_p^2}\right] \times \left[\left(\frac{char^\bullet}{char}\right)^{1/3} - 1\right]^{-1} \ (\text{kg } H_2O/\text{m}^3 \cdot \text{s}) \quad , \tag{57}$$

where char is the local char density and $char^\bullet$ is the maximum char density that can be produced in the local particle shell. If char = $char^\bullet$, we set R_{7b} to 10^{30}. If char = 0, we set R_{7b} to 0.

The reaction rate between cnar and steam is determined from

$$R_{7a} = 1.5\ \sqrt{P_{H_2O}} \cdot char \cdot 3.14 \times 10^3 \times e^{(-22140/T)}\ (\text{kg } H_2O/\text{m}^3 \cdot \text{s}) \quad , \tag{58}$$

where P_{H_2O} is the partial pressure of H_2O vapor in the bulk gas stream.

The total reaction rate is then

$$R_7 = \frac{R_{7a}\ R_{7b}}{R_{7a} + R_{7b}}\ (\text{kg } H_2O/\text{m}^3 \cdot \text{s}) \tag{59}$$

and the amount of H_2O reacted during a time step Δt is

$$\Delta H_2O = R_7 \cdot \Delta t \cdot \Delta \Omega_s\ (\text{kg } H_2O) \quad , \tag{60}$$

where $\Delta\Omega_s$ is the particle shell volume. The amount of char consumed and the quantities of CO and H_2 produced are then found from

$$\Delta \text{ char} = 0.667\ \Delta H_2O \quad (kg)\ ,$$
$$\Delta H_2 = 0.1119\ \Delta H_2O \quad (kg)\ ,$$
$$\Delta CO = 1.5548\ \Delta H_2O \quad (kg)\ . \qquad (61)$$

The H_2O consumed is subtracted from the total H_2O while the H_2 and CO produced are added to the bulk gas stream. The amount of char consumed is subtracted from the total char in the particle shell. Energy absorbed by this reaction is 7.29×10^6 J/kg · H_2O consumed.

Water-Gas Shift

$$CO + H_2O \underset{K_2}{\overset{K_1}{\rightleftharpoons}} CO_2 + H_2$$

This reaction can change the composition of the product gas. The reaction can occur in either direction depending on the local gas stream temperature and the relative concentration of the reactants.

The rate of reaction of H_2O is given by

$$\Delta H_2O = -\Delta t \cdot K_1 \cdot \{[CO] \cdot [H_2O] - K_2 \cdot [CO_2] \cdot [H_2])\ \text{(moles)}\ , \qquad (62)$$

where
[CO] = molar concentration of CO in gas stream,
$[H_2O]$ = molar concentration of H_2O in gas stream,
$[CO_2]$ = molar concentration of CO_2 in gas stream,
$[H_2]$ = molar concentration of H_2 in gas stream,

and

$$K_1 = 375. \times e^{(-7300/T)}\ (s^{-1})\ , \qquad (63)$$
$$K_2 = 58.82\ e^{(-4400/T)}\ . \qquad (64)$$

Heat of reaction is 2.29×10^6 J/kg · ΔH_2O.

As in all reactions in WAFE-OS, we check to insure that reactions do not consume more substrate than is available. This prevents one source of non-conservation of mass and energy.

Coking

An additional decomposition can occur in the oil that remains inside shale particles during pyrolysis. This process is called coking. The coking reaction is approximated by

$$1 \text{ kg oil} \xrightarrow[K_c]{} .0604 \text{ kg } H_2 + .0431 \text{ kg } H_2O + .1927 \text{ kg } CH_4 + .7038 \text{ kg char} \qquad (65)$$

where $K_c = 3.1 \times 10^7 \times e^{(-17681/T)}\ s^{-1}$. (66)

The extent of coking depends on the heating rate history of the shale at any point, since that controls the fraction of oil that remains in the shale during and after kerogen pyrolysis.

Model Check-Out

The fluid flow portion of the model has been compared with two-phase analytic similarity solutions for a number of boundary and initial conditions with excellent agreement. (For example, Fig. 2 shows comparison with one similarity solution.) It has also been checked against several sets of experimental data. In one experiment, super-heated steam was injected into a vertical column of cold, initially dry sand. Temperature and pressure were recorded at various depths in the column. The calculations agree well with the data. In another experiment, hot N_2 was injected into cylindrical samples of partially saturated, crushed tuff. Inflow rates, injection pressure and temperature, and temperatures at points within the sample were recorded. The model calculations showed good agreement with the data. Details of these and other comparisons will be available in a separate report.

We have made a number of check-out calculations to insure that the new features (temperature structure inside particles and oil shale chemistry) are working properly. Figure 3 compares numerical and analytic solutions for diffusion of heat into spherical particles at several times. Time has been non-dimensionalized by multiplying by κ/R_p^2, where κ is the thermal diffusivity. Temperature and radius have been normalized. The three solutions shown correspond to early, intermediate, and late times. In each case, surface temperature was held fixed. In one numerical calculation, five internal shells of equal volume were used (the +'s); in a second calculation, five internal shells of equal thickness (the X's) were used; and the final calculation used a single internal shell (the circles on the ordinate axis).

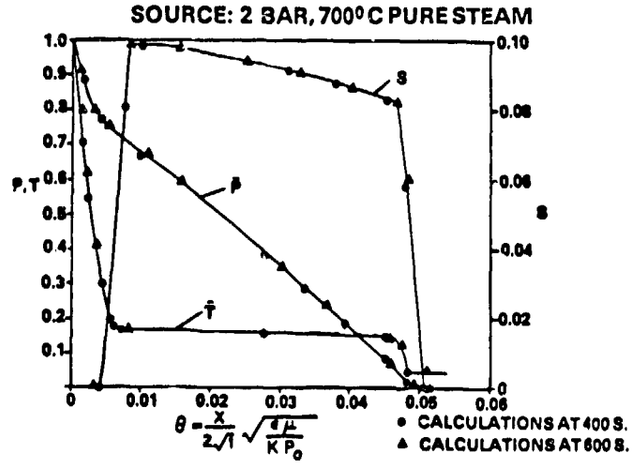

Fig. 2. Similarity solution for 0% initial saturation.

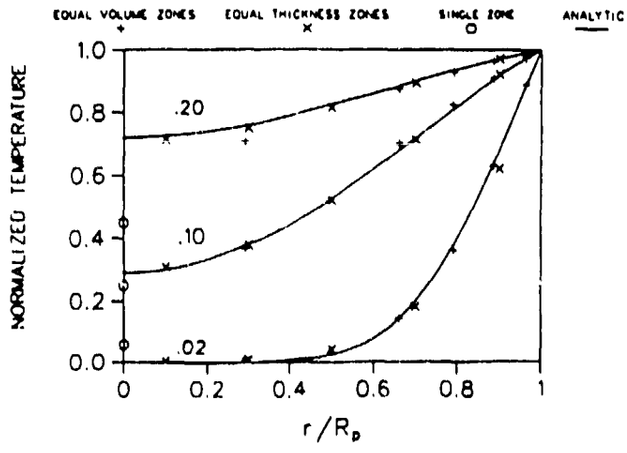

Fig. 3. Temperature in a sphere, analytic vs calculated, at dimensionless times $(\kappa t/R_p^2)$ = .02, .10, and .20.

It appears that five shells of equal thickness provides good accuracy. In other calculations, initial pore fluid temperature and rock temperature were set to different values. In all cases, the rock and fluid temperatures reached a common equilibrium temperature equal to that required by energy conservation.

Another series of calculations exercised the kerogen pyrolysis and carbonate decomposition sections of WAFE-OS. In this study, the inert fluid bathing the shale particles was heated at a constant rate. The rates of production of kerogen products (methane, hydrogen, oil, steam, CO_2, and CH_x, which represents several C_2 and C_3 products) were monitored. Figures 4 and 5 show the production rates (vs fluid temperature) of oil and H_2, respectively, for two heating rates--12°C/hr and 120°C/hr. Particle radius for these calculations was 0.1 cm. Material properties used are given in Table I.

Figures 6 and 7 plot production rates for oil and H_2 vs fluid temperature when the bathing fluid is heated at 120 °C/hr. Here, the effect of particle radius is shown. As particle radius increases, production is shifted to higher fluid temperatures, and the curves have changed qualitatively. This change reflects the delay in conduction of heat into larger particles. No combustion was allowed for this test.

Table I. Material Properties

Grade	0.1 ℓ/kg (14.6% wt kerogen)
Density	2.25×10^3 kg/m^3
Thermal conductivity	1 J/m·s
Specific heat	1.2 kJ/kg.s
Heat transfer coefficient	8 J/m^2·s
Dolomite	30% wt
Calcite	17% wt

The effect of particle size on consumption of char in an oxygenated atmosphere is shown in Fig. 8. As expected, larger particles take longer to burn. Oxygen has difficulty diffusing deep into large particles. The rate at which the sharp burn front moves into a particle slows down as the burn radius diminishes. Further details and additional figures of these checkout runs can be found in Ref. (8).

COMPARISON WITH EXPERIMENT

The preceding exercises indicate that the various parts of the WAFE-OS model are functioning properly and generate reasonable results. Testing of the entire model at one time can be done in several ways. (Since

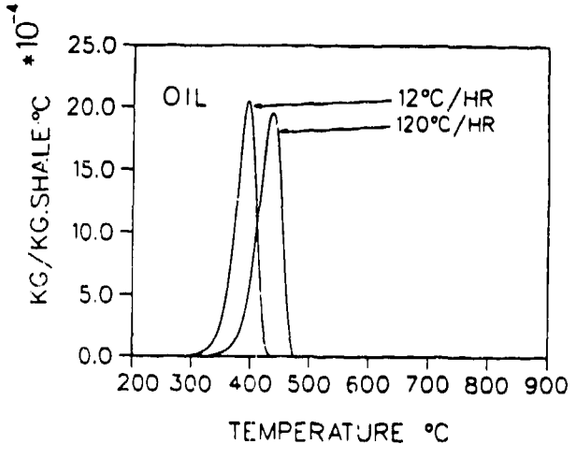

Fig. 4. Oil production rates from kerogen for different heating rates.

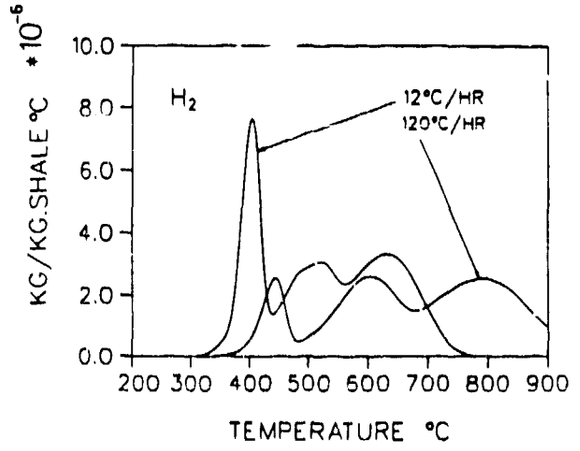

Fig. 5. H_2 production rates from kerogen for different heating rates.

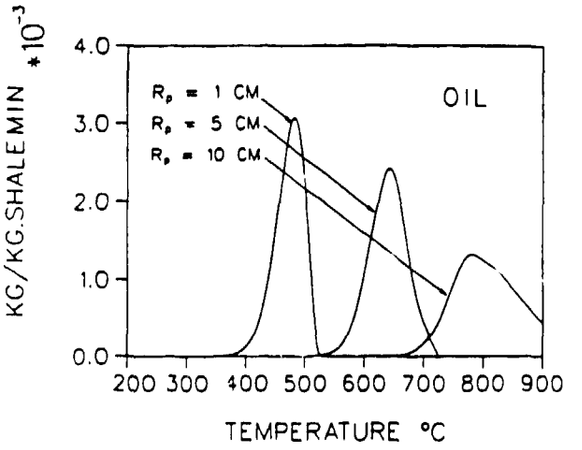

Fig. 6. Oil production rate dependence on particle radius at constant heating rate of 120°C/h.

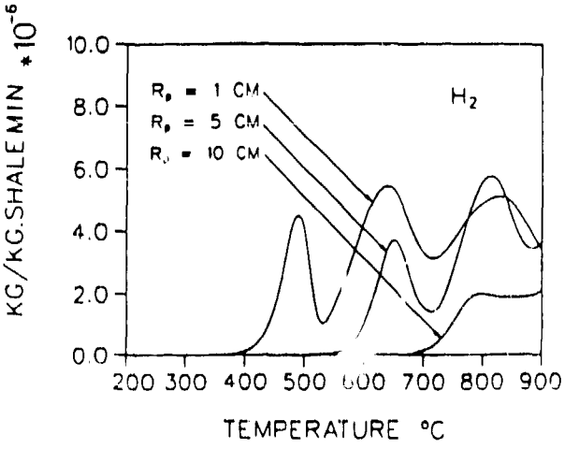

Fig. 7. H_2 production rate dependence on particle radius at constant heating rate of 120°C/h.

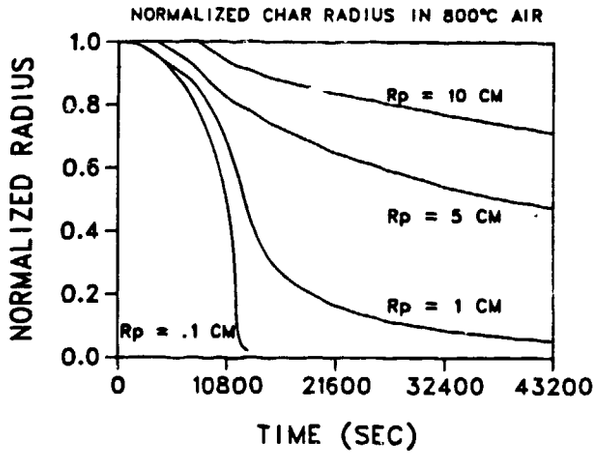

Fig. 8. Effect of particle size on consumption of char in an oxygenated atmosphere.

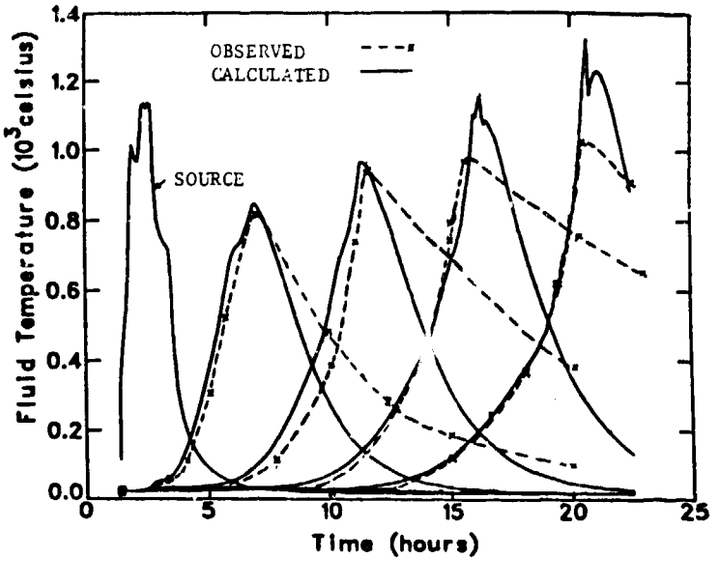

Fig. 9. Comparison of calculated with observed temperature histories for Run S-17. Higher peak calculated temperatures and lower late-time calculated temperatures are believed due to effect of wall heater.

no analytic solutions to a retorting process are known, this avenue is not available.) Benchmarking, that is, comparison to other code calculations, is possible. Comparison of WAFE-OS to results generated by the LLNL one-dimensional model would be a good benchmarking test. Such a comparison is planned in the near future.

The most important tests of WAFE-OS (or of any model) are comparisons with actual experimental data. We are fortunate in that a great deal of experimental shale retorting data is available. Many documented one-dimensional retorting experiments have been conducted at LLNL. We have compared WAFE-OS to one of these, designated as Run S-17 (11). We plan additional comparisons in the future with other runs.

Run S-17 was a combustion run using an air and nitrogen mixture source. Table II indicates relevant material and geometric properties of the experiment. Table III describes the source conditions used.

The calculation compared favorably with the experiment. Figure 9 compares observed centerline temperature histories with calculated values. The curves are reasonably close. The calculated curves are somewhat higher than observed. In the experiment, heat loss at the walls of the vessel was not entirely controlled. Temperatures measured in the wall and in the shale next to the wall were as much as 100°C lower than centerline. This wall heat loss was not included in the calculation. A two-dimensional calculation that includes wall heat loss will be done. Oil yield was measured as 88 volume (although on another page of Ref. (11) it is given as 92%). Our code calculation predicted an oil yield of 91%. This again is probably influenced by the higher calculated temperatures. Retorting rate is also very close to the measured value of about 1.73 m/day. Figure 10 shows volume percent of one of the exit gases as a function of time.

Table II. Characteristics of Run S-17

Shale charge	123.2 kg
Fischer assay	0.104 ℓ/kg
Void fraction	47%
Charge length	1.46 m
Particle size	- 2.54 + 1.3 cm
Effective particle size	1.8 cm
Length of run	22 h
Mineral carbon	4.57% wt
Bulk shale density	2.22 x 10^3 kg/m^3
Heat transfer coefficient B used in calculation	8 J/m^2·s
Thermal conductivity of shale	0.48 J/m·s·°C
Specific heat used	1 kJ/kg·°C

Table III. Inflow Composition Used in Calculation

Time (h)	Air (% Vol.)	N_2 (% Vol.)	Flow (ℓ/s)	Temp. (°C)
1.4 - 2.73	100	0	0.3	1200
2.73 - 3.44	100	0	0.845	1200
3.44 - 23.44	50	50	0.845	31

APPLICATIONS

The applications of a fully-coupled, two-dimensional retorting model are numerous. It can be used to evaluate various ignition strategies; look at the effects of leaks and water infiltration; determine the impact of non-uniformities in porosity, rubble size, grade, and composition; show the influence of buoyancy and condensation; and compute the effect of retort geometry.

Our effort until very recently has focused on creating a versatile tool, WAFE-OS. Application of the model to these varied concerns is only now beginning.

Two-Dimensional Example

In this section, a sample two-dimensional application is described. It demonstrates the capabilities of WAFE-OS. Figure 11 shows the basic retort geometry considered in the example. The retort is assumed to have a rectangular cross-section whose width is 15 m and whose height is 33 m, the top 3 m of which is a void space. Several types of non-uniformities have been included in the column. On the right side, we

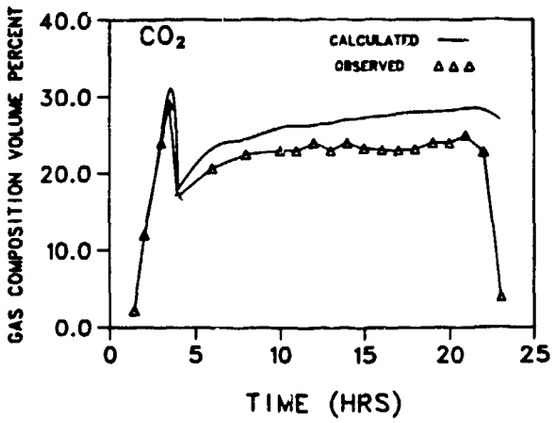

Fig. 10. Calculated and observed CO_2 content of exit gas.

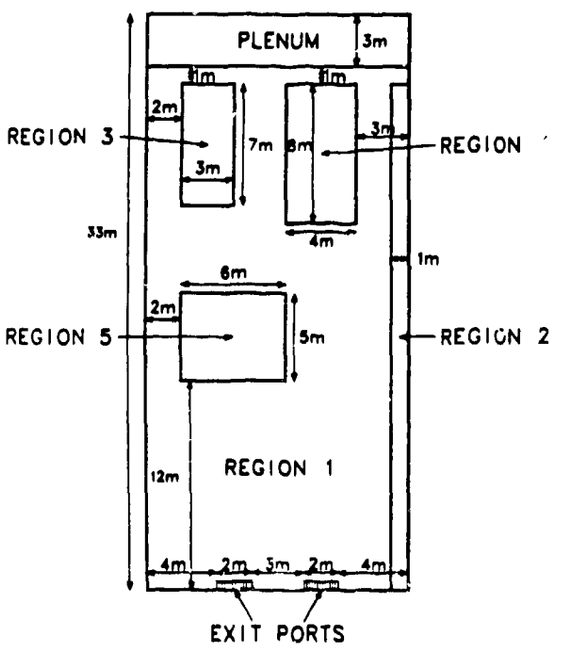

Fig. 11. Two-dimensional geometry used in sample calculation.

assume a high permeability channel. Near the channel in the upper part is a region of high permeability, low porosity, and large rubble size. In the upper left area is a region of low permeability due to the presence of small rubble size. In the lower part of the retort, we have included a region of low-grade shale. The sides of the retort are impermeable. Two exit ports are included in the floor. Inflow gases are deposited in the plenum void at the top. (Injection of in-flow gases at discrete points is allowed in the WAFE-OS model, however.) Table IV indicates the relevant material properties used in the calculation and Table V gives the inflow gas composition and energy. This example is not intended to represent any particular site. The non-uniformities chosen are believed typical of what is found in the field. The particular values of permeability, etc., are only estimates.

Table IV. Material Properties Used in Calculation

	Region				
	I	II	III	IV	V
Permeability (Darcys)	50	250	10	200	50
Porosity	.25	.30	.35	.10	.25
Average particle diam (cm)	15	20	2	30	15
Heat transfer coefficient β ($J/m^2 \cdot s$)	8	8	8	8	8
Rubble density (kg/m^3)	2300	2300	2300	2300	2300
Specific heat ($kJ/kg \cdot °C$)	1	1	1	1	1
Thermal conductivity ($J/m \cdot °C \cdot s$)	0.5	0.5	0.5	0.5	0.5
Kerogen, %wt	15	15	15	15	5
Dolomite, %wt	21	21	21	21	22
Calcite, %wt	12	12	12	12	15

1.0 Darcy = $9.87 \times 10^{-13} m^2$

Table V. Inflow Composition and Energy

Time (h)	O_2 (% Vol.)	N_2 (% Vol.)	Steam (% Vol.)	Flow Rate (moles/$m^2 \cdot s$)	Temp. (°C)
0-24	0	35.0	65.0	.43	800
24-	12.6	47.4	40.0	1.7	70

Results

Multi-dimensional, multi-component reactive flow models can generate an enormous amount of information. Automatic graphic display of results greatly reduces the task of interpreting such calculations.

In the present example, the simple-minded ignition strategy used did not result in uniform heating and ignition across the retort. The regions of highest permeability (Regions 2 and 4 in Fig. 11) heated up faster than the other regions and ignition occurred there first. Our inflow changed to a cold air-steam mixture that prevented the shale outside Regions 2 and 4 from igniting. Eventually, the burning fronts may spread into the unignited regions. This calculation was terminated shortly after ignition started because of the poor ignition pattern. The calculation will be done again with a different inflow strategy. However, the results from this brief run are of some interest.

Figures 12 and 13 show the fluid temperature contours before and after ignition, respectively. The temperature peaks in Fig. 13 are clearly seen in the channel and in the large block regions. Liquid saturation contours are shown in Figs. 14 and 15 for pre- and post-ignition conditions. Liquid is accumulating in the low-permeability, small-particle region and in the shale immediately adjacent to the channel. No liquid is present in the hot shale above 25 m (Fig. 15). As the retort heats up, liquid will slowly move out and vapor will not be able to condense.

In the remaining figures, which compare molar concentration contours pre- and post-ignition for various pyrolysis and carbonate decomposition and combustion product gases, the effect of non-uniform properties is very obvious. CO_2 production is illustrated in Figs. 16 and 17. Pre-ignition CO_2 production is mainly in Regions 2 and 4, which are hottest. In Fig. 17, CO_2 is coming mainly from combustion and carbonate decomposition. The left side

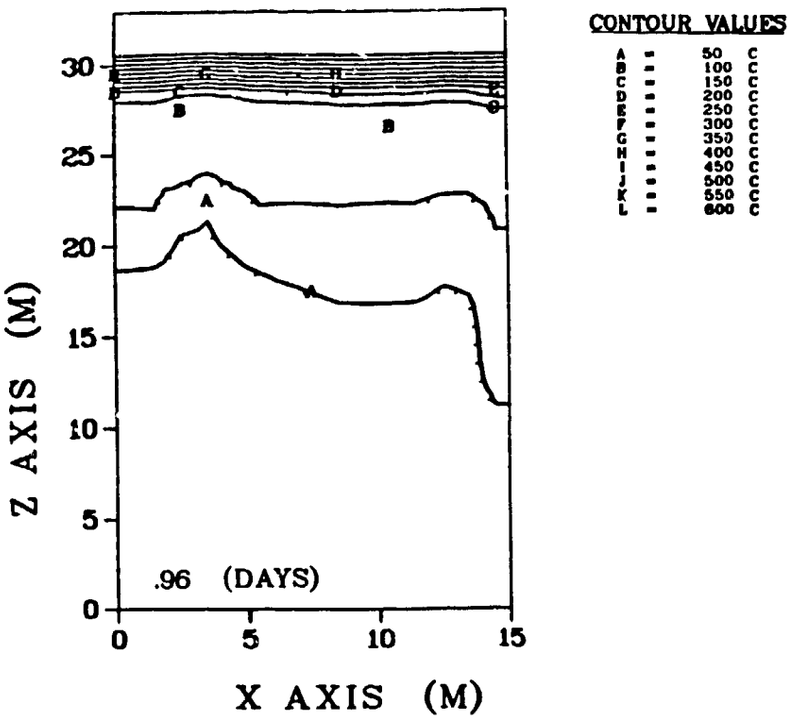

Fig. 12. Calculated pre-ignition fluid temperature field.

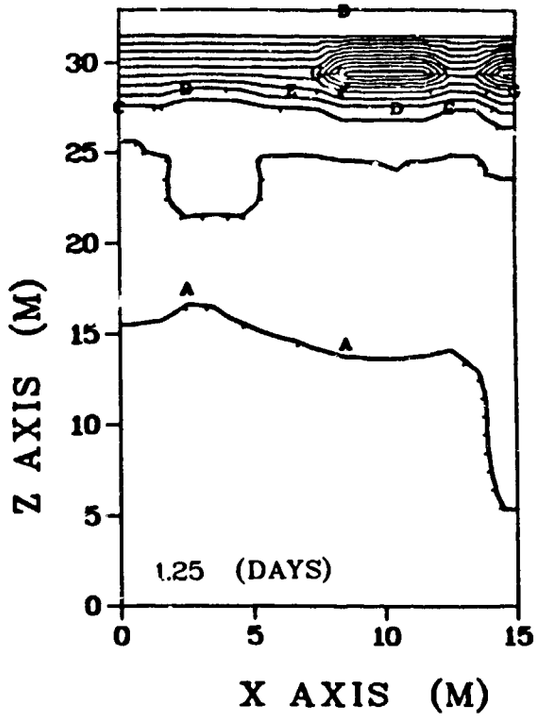

Fig. 13. Calculated fluid temperature field after ignition.

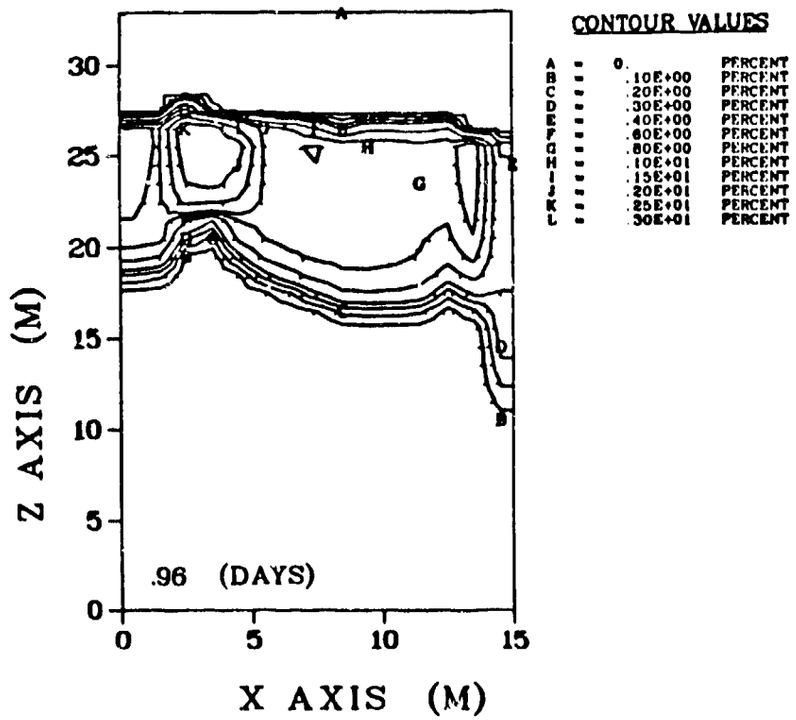

Fig. 14. Water saturation distribution shortly before ignition.

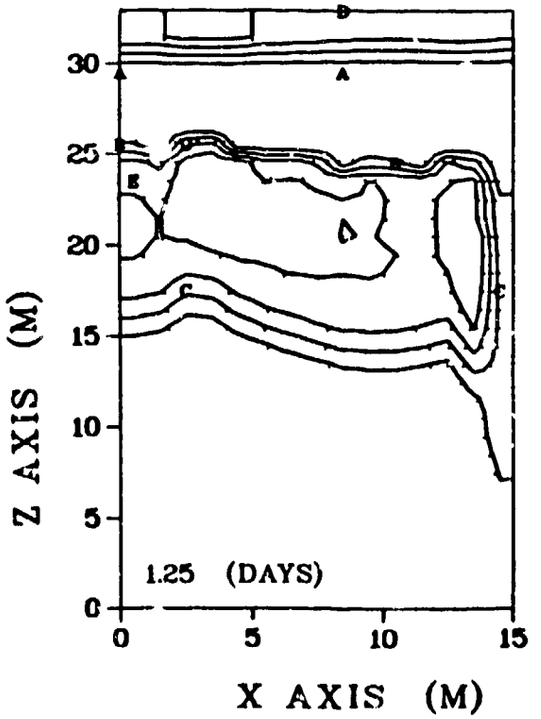

Fig. 15. Water saturation distribution shortly after ignition.

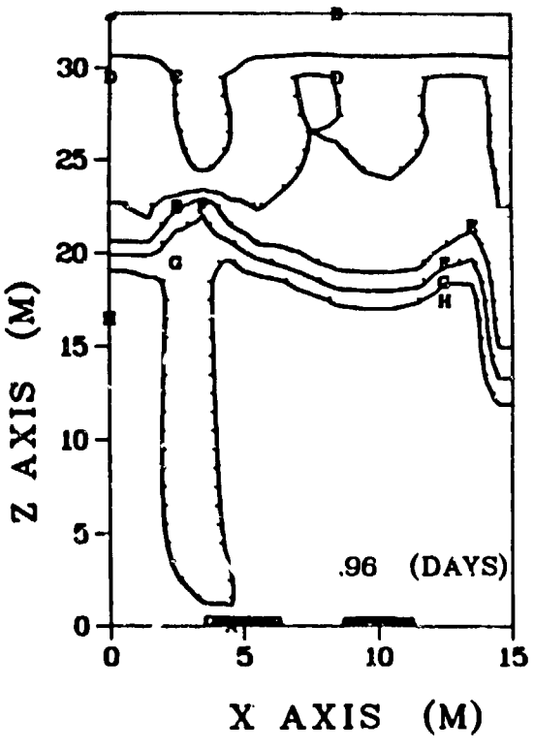

Fig. 16. Calculated CO_2 molar concentration shortly before ignition.

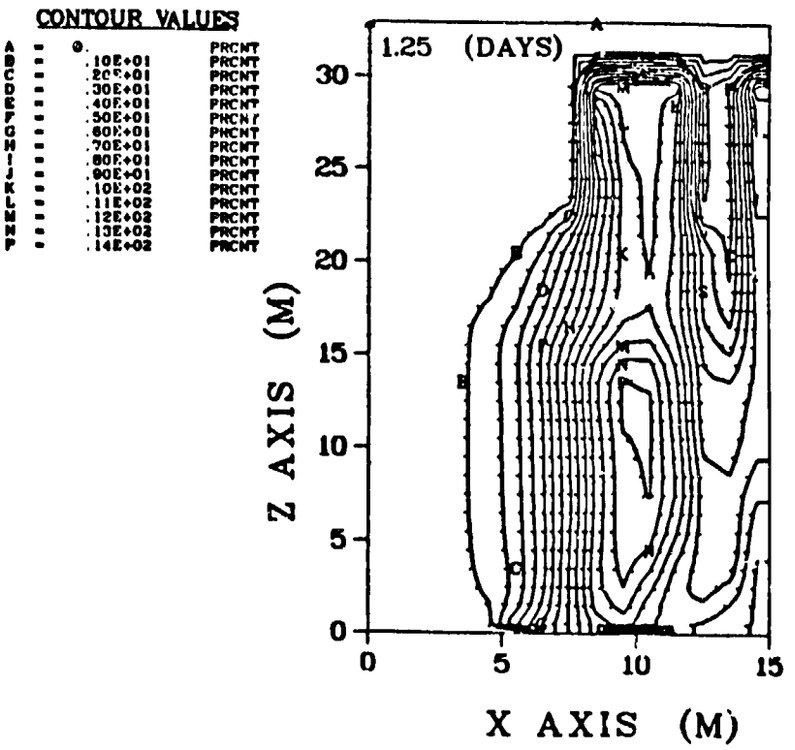

Fig. 17. Calculated CO_2 molar concentration shortly after ignition.

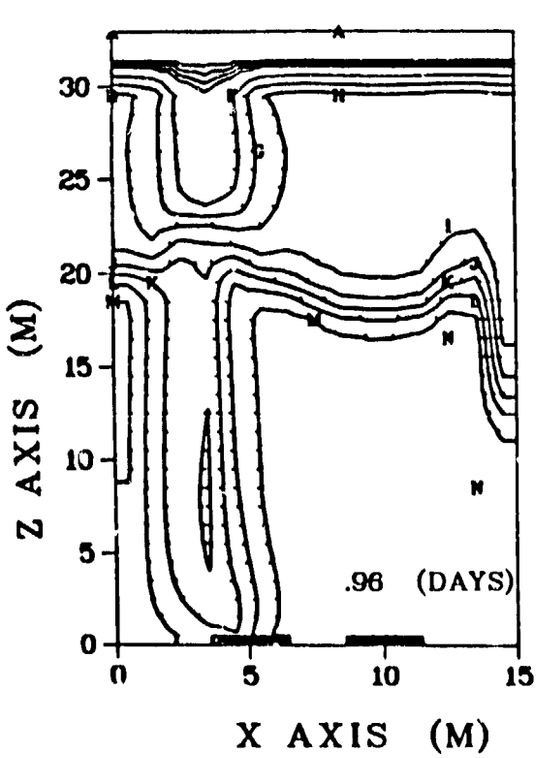

Fig. 18. Calculated oil vapor molar concentration before ignition.

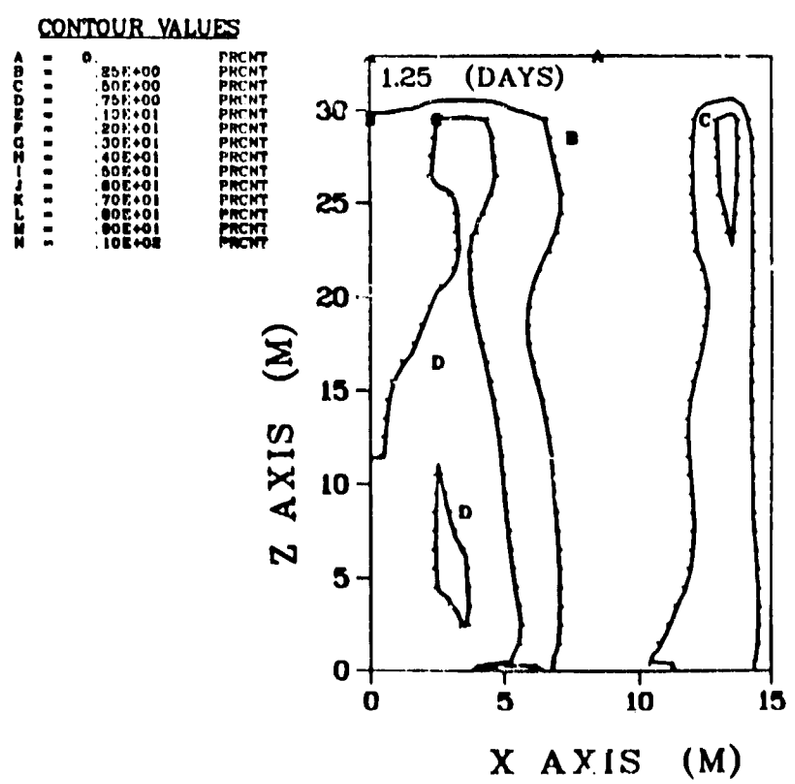

Fig. 19. Calculated oil vapor molar concentration after ignition.

of the retort is cooling off and CO_2 generation is virtually stopped. Figures 18 and 19 show oil vapor concentration contours. In Fig. 18, oil generation is strongest in the upper right-hand area. Downstream of that region, the concentration is higher because of mixing and because of the slower flow there. After ignition (Fig. 19), oil is of course depleted in and below the combustion zones. Oil production is continuing in other hot parts of the retort. Plots of H_2, CH_4, and CH_x are not shown because they are very similar to the oil vapor patterns. This example, although incomplete, exercises almost all of the capabilities of the WAFE-OS model. Future work should reveal to us the sensitivity of important parameters such as total oil yield to non-uniformities in retort properties.

CONCLUSION

We have described a time-dependent, two-dimensional oil shale retorting model that fully couples retorting chemistry with flow dynamics. The computer code WAFE-OS, which numerically solves the equations of the model, has been compared with analytic solutions and experimental data with satisfactory agreement. A sample two-dimensional calculation has been described that demonstrates the capabilities of the model. The model can be used to examine the effects of ignition strategies, the effects of problems such as water infiltration, the effect of non-uniformities in rubble size, grade, permeability, etc., on retort efficiency, and the impact of buoyancy in horizontal (and vertical) retorting. Future work will concentrate on exploring these various applications.

REFERENCES

1. Braun, R. L., "Mathematical Modeling of Modified In Situ and Above-Ground Oil Shale Retorting," Lawrence Livermore National Laboratory report UCRL-53119 (January 1981).

2. Tyner, C. E., and Hommert, P. J., "Numerical Modeling of a True In Situ Oil Shale Retort," Sandia National Laboratories report SAND-78-1306 (January 1979).

3. George, J. H., Harris, H. G., and Thomas, J. W., "Mathematical Modeling of In Situ Oil Shale Retorting Processes," Proc., Conf. on Fluid Mechanics in Energy Conversion, SIMS, Alta, UT, 1979.

4. Cook, T. L., Travis, B. J., Harlow, F. H., Bartel, T. J., and Tyner, C. E., "Heat and Mass Transfer in Porous Media," Proc., 14th Oil Shale Symposium, Colorado School of Mines, Golden, CO, April 22-24, 1981.

5. Hommert, P. J., and Tyner, C. E., "Model Capabilities for In Situ Oil Shale Recovery," Sandia National Laboratories report SAND-80-572 (1981).

6. Travis, B. J., "WAFE, A Model for Multi-Phase, Multi-Component Mass and Heat Transport in Porous Media," Los Alamos National Laboratory report, LA-UR-80-611 (1982).

7. Campbell, J. H., and Burnham, A. K., "Reaction Kinetics for Modeling Oil Shale Retorting," Lawrence Livermore National Laboratory report UCRL-81622 (1979).

8. Travis, B. J., Hommert, P. J., and Tyner, C. E., WAFE-OS: A Two-Dimensional Numerical Model of In Situ Oil Shale Retorting, Los Alamos National Laboratory report LA-UR-82-1155 (1982).

9. Dullien, F. A. L., Porous Media: Fluid Transport and Pore Structure, Academic Press, New York, 1979.

10. Bear, J., Dynamics of Fluids in Porous Media, Elsevier Press, New York, 1972.

11. Sandholtz, W. A., Ackerman, F. J., Raley, J. H., Carley, J. F., and Tripp, L. J., "LLL Oil Shale Project, Small Retort Run Summary, Run S-17," Lawrence Livermore National Laboratory report UCID-18899 (December 1980).